Distinct Universality Classes of Domain Wall Roughness in Two-Dimensional Pt/Co/Pt Films

Kyoung-Woong Moon,[1] Duck-Ho Kim,[1] Sang-Cheol Yoo,[1,2] Cheong-Gu Cho,[1] Sungmin Hwang,[1] Byungnam Kahng,[1] Byoung-Chul Min,[2] Kyung-Ho Shin,[2] and Sung-Bong Choe[1,*]

[1]*CSO and Department of Physics, Seoul National University, Seoul 151-742, Republic of Korea*

[2]*Center for Spintronics Research, Korea Institute of Science and Technology, Seoul 136-791, Republic of Korea*

(Received 1 November 2012; published 7 March 2013)

We demonstrate here that the current-driven domain wall (DW) in two dimensions forms a "facet" roughness, distinctive to the conventional self-affine roughness induced by a magnetic field. Despite the different universality classes of these roughnesses, both the current- and field-driven DW speed follow the same creep law only with opposite angular dependences. Such angular dependences result in a stable facet angle, from which a single DW image can unambiguously quantify the spin-transfer torque efficiency, an essential parameter in DW-mediated nanodevices.

DOI: 10.1103/PhysRevLett.110.107203 PACS numbers: 75.78.Fg, 75.76.+j, 68.35.Rh, 75.60.Ch

Interfaces exhibit diverse phenomena and their statics and dynamics govern many key features of such phenomena. Because of the common nature of interfaces, there often exists universality among various dissimilar phenomena, allowing classification of many phenomena into a small number of universality classes. Such universality classes are determined by a variety of factors, but the core factor is the competition among forces acting on the interfaces, i.e., the external driving forces vs the internal disorder- and interface-induced forces. Therefore, to better understand the nature of the universality classes, it is challenging to manipulate such competition, possibly by applying several distinct external forces onto a given system.

Magnetic systems offer a platform to achieve such experiments with different driving forces. Magnetic domain walls (DWs)—the interface between two different magnetic domains—exhibit power-law scaling behaviors in their roughness and motion. Magnetic fields have long been used as a DW driving force for scaling experiments, revealing the Barkhausen [1,2] and creep [3–7] scalings. Recently, electric currents have been proposed as another DW driving force. This driving force is caused by spin-transfer torque (STT) via the transferring of spin angular momentum from conduction electron spins to magnetic moments [8–10]. The existence of these two forces raises the possibility that different universality classes may be realized in a single system depending on the driving forces. Recent experiments [11,12] have demonstrated different universality classes of the DW creep, depending on disorder types and major STT components. Note that all the current-driven experiments up to now have been carried out only on quasi—one-dimensional wire geometries, in contrast to the field-driven experiments that have been extensively carried out on two-dimensional films [1–6] and recently extended to one-dimensional wires [7]. Such one-dimensional geometries allow the detection of the DW position only, without any information about the roughness, though the roughness plays a crucial role in the determination of the DW creep scaling since the motion takes place by thermal activation of rough DW segments. To get information about the roughness, it is thus required to carry out experiments in two-dimensional systems. By accomplishing such current-driven experiments in two-dimensional systems, here we show that the study of the roughness reveals hitherto unknown features of the DW motion.

Metallic ferromagnetic Pt/Co/Pt films [12] with perpendicular magnetic anisotropy are chosen as the two-dimensional system for this study. 5.0-nm Ta/2.5-nm Pt/0.3-nm Co/1.5-nm Pt films are deposited on a Si substrate with a 100-nm-thick SiO_2 layer by dc-magnetron sputtering. 3.0-mm-wide and 0.6-mm-long magnetic structures are defined by photolithography, after which 100-nm-thick Au electrodes are stacked onto both ends of the structure for current injection. A copper plate with large heat capacity (~ 100 J/K) is attached to the sample for fast heat dissipation. The current flows along the length direction as indicated by the white arrow in Fig. 1(a). The current density J is calculated under an assumption of uniform current distribution through the conducting layers, since the layers are much thinner than the electron mean free path. The magnetic field H is applied perpendicular to the film as shown by the white symbol in Fig. 1(e). The polarities of the current and the field are defined as each positive polarity corresponds to the force along the $+h$ direction. The DW images are observed by a magneto-optical Kerr effect microscope exactly at the center of the films in order to minimize the Oersted field (< 0.01 mT) across the field of view. To create a linear DW, the film is first saturated by a magnetic field larger than the coercive field and then a reversed magnetic field smaller than the coercive field is applied. At this instant, a laser beam is focused onto a small spot (5 μm in diameter) to reduce the coercive field at the spot and thus, to create a reversed domain. By scanning the sample stage along a desired path, any shape of the reversed domain can be written.

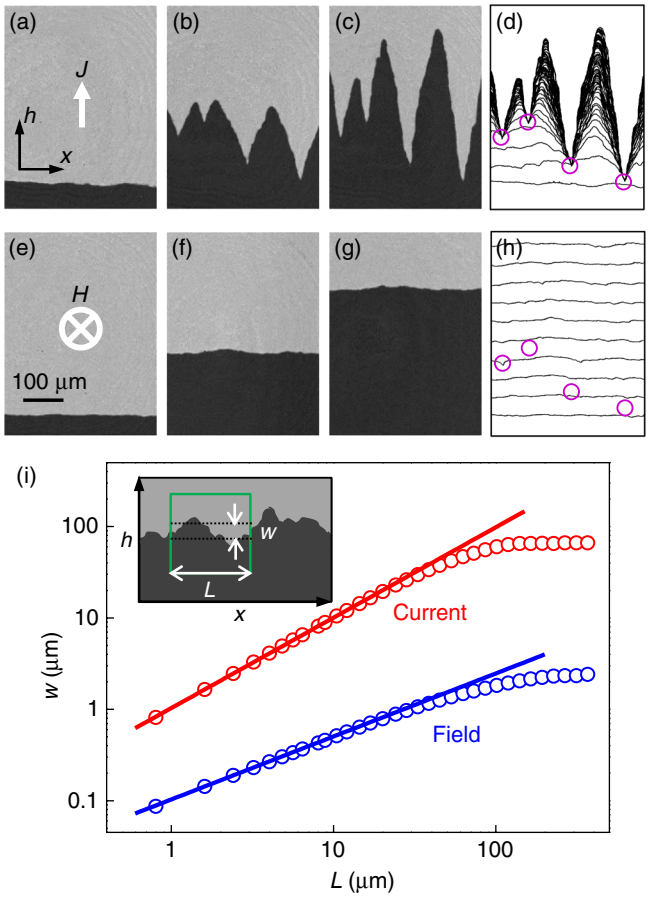

FIG. 1 (color online). Magnetic domain images taken at (a) 0 s, (b) 20 min, and (c) 4 hr after the application of J (1.0×10^{10} A/m^2). (d) Time-resolved DW lines superimposed sequentially with a constant time step (3 min). Images taken at (e) 0, (f) 10, and (g) 20 min after the application of H (1.0 mT). (h) Time-resolved DW lines superimposed sequentially with a constant time step (3 min). The purple circles in (d) and (h) designate the strong pinning sites that appeared in the current-driven motion. (i) Log-log scaling plot between the DW segment length L along the x axis and the roughness amplitude w along the h axis for DWs driven by the current (red) and field (blue). w is defined as the standard deviation of the roughness fluctuation over the length L. Each symbol is obtained by sampling more than 1000 times. The solid lines show the best linear fit.

The current-driven roughness growth in these films is depicted in Figs. 1(a)–1(d). Figure 1(a) shows a linear DW initially created by the thermomagnetic writing scheme. By injecting current, the linear DW starts to develop the shape of mountains with a constant slope as seen by Figs. 1(b) and 1(c). Figure 1(d) summarizes this evolution by superimposing the DW lines sequentially with a constant time step. We observe this behavior for more than 10 samples under examination, over the range of J between 0.7 and 2.2 times 10^{10} A/m^2. This behavior is distinct from that of the field-driven roughness as shown by Figs. 1(e)–1(h), where the DW sweeps with a constant speed without a significant change in the shape of roughness.

These distinct DW shapes belong to different universality classes. Figure 1(i) depicts the log-log plot between the DW segment length L along the x axis and the roughness amplitude w along the h axis. The linear relation indicates the power-law scaling $w \propto L^{\zeta}$, where ζ is labeled the roughness exponent [13]. The best fit quantifies that $\zeta_J = 0.99 \pm 0.01$ for the current and $\zeta_H = 0.68 \pm 0.04$ for the field. The exponent ζ_H ($\neq 1$) indicates the conventional self-affinity of the field-driven DW roughness as already well established in a number of studies with $\zeta_H = 2/3$ [4–6]. In contrast, the current-driven exponent ζ_J ($\simeq 1$) corresponds to the self-similarity in the present scaling range. Thus, very surprisingly, the same DW exhibits distinctive roughness scalings between the self-affinity and self-similarity in the same system depending on driving forces.

In the current-driven cases, the shape of the mountains is developed by the pinning of DWs at several strong pinning sites as indicated by purple circles in Fig. 1(d). Once the structure is fully developed, the strength of pinning is so strong that the DW is barely depinned over the measurement time range of up to a few days. By contrast, such strong pinning does not appear in the field-driven case as shown by Fig. 1(h). This suggests that the DW responds differently to pinning sites depending on what the driving force is.

In quenched disorder systems such as magnetic media, universal behaviors of the interface dynamics are governed by the quenched Kardar-Parisi-Zhang (KPZ) equation [13,14], which describes the temporal change of the interface height $h(x, t)$ at the position x and time t by $\partial h/\partial t = V_0 + \nu(\partial^2 h/\partial x^2) + (\lambda/2)(\partial h/\partial x)^2 + \eta_q$. The first term denotes the mean speed. The second term describes relaxation caused by the tension ν. The third term is called the KPZ nonlinear term and induces growth ($\lambda > 0$) or decay ($\lambda < 0$) along the local normal to the interface, depending on the sign of the coefficient λ. The fourth term reflects the noise induced by the local disorders and thermal fluctuations.

The KPZ equation predicts qualitatively different interface dynamics depending on the sign of λ. A scaling analysis predicts the conventional self-affine roughness for a positive λ [13,15]. However, for a negative λ, the interface forms a typical roughness—called a facet [16,17]—in the shape of mountains with a constant slope, which is truly accordant with our observation. It is thus natural to deduce that the DW driven by the current (field) is described by the KPZ equation with a negative (positive) λ.

The opposite sign of λ readily explains the different pinning mechanisms [17]. When a driven interface meets a pinning site, the interface bends at around the pinning site and thus, the slope $|\partial h/\partial x|$ adjacent to the pinning site increases accordingly. At this instant, for a positive λ, the KPZ nonlinear term adds a force positively to the driving force. It thus enhances the bending recursively

and consequently, assists depinning. On the contrary, a negative λ suppresses the bending via the force opposite to the driving force. Since more bending with a larger driving force further enhances the negative KPZ force, a significantly large force is required to overwhelm the KPZ force to trigger depinning.

Driving force dependence appears also in the slope-dependent DW displacement. For this, a linear DW is initially prepared with an angle θ ($= \tan^{-1}[\partial h/\partial x]$) and then subjected to either a magnetic field or current pulse. Figure 2 depicts the results for the current (a)–(d) and field (e)–(h). Each image is obtained by adding two images before and after the translation and thus, each image shows two DWs simultaneously. For the field-driven motion, the displacement $\Delta h_\perp$ normal to the DW is found to be invariant irrespective of θ. This behavior is due to the rotation

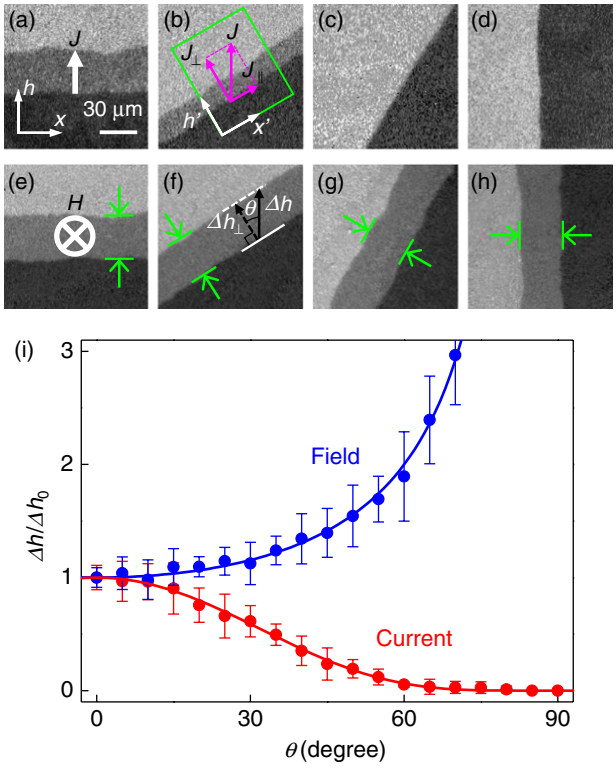

FIG. 2 (color online). Displacement driven by a current pulse (1.0×10^{10} A/m^2, 150 s) for DWs with different θ, (a) 0, (b) 30°, (c) 60°, and (d) 90°. Displacement driven by a magnetic field pulse (1.0 mT, 150 s) for DWs with different θ, (e) 0, (f) 30°, (g) 60°, and (h) 90°. The purple arrows in (b) illustrate the decomposition of J into the parallel $J_\parallel$ and normal $J_\perp$ components. The green window in (b) exemplifies the new coordinate axes—x' and h'—parallel and perpendicular to the DW. The equilength green arrows in (e)–(h) guide $\Delta h_\perp$. The white solid and dashed lines in (f) indicate the DWs before and after the displacement, respectively. The black solid and dashed arrows in (f) depict the displacements Δh and $\Delta h_\perp$, respectively. (i) Plot of $\Delta h/\Delta h_0$ with respect to θ for DW motion driven by the current (red) and field (blue). The error bars correspond to the standard deviation from data obtained by sampling 10 times.

symmetry with respect to the axis parallel to the applied field H. On the contrary, for the current-driven motion, $\Delta h_\perp$ decreases as θ increases as we discuss further below. These angular dependences are summarized in Fig. 2(i). We observe the angular dependences for 3 different samples with the range of J between 1.0 and 3.4 times 10^{10} A/m^2. The ordinate is scaled as the displacement Δh along the $+h$ axis, normalized by Δh_0 for $\theta = 0$. The plot shows opposite dependences for the field (positive) and current (negative). For the field-driven case, the data fit to a $1/\cos\theta$ function, which is attributed to the relation $\Delta h_\perp = \Delta h \cos\theta$ with a constant $\Delta h_\perp$ ($= \Delta h_0$) as illustrated in Fig. 2(f).

The different slope dependence is a direct indicator of the opposite sign of λ. When Δh is converted into the DW speed $V(= \Delta h/\Delta t)$ using the pulse duration Δt, the field-driven $1/\cos\theta$ dependence indicates a positive λ, since the Taylor expansion of V with respect to $\partial h/\partial x$ gives the first leading term as $(V_0/2)(\partial h/\partial x)^2$, which is identical to the KPZ nonlinear term with $\lambda = V_0$ ($= \Delta h_0/\Delta t > 0$). For the current-driven case, on the other hand, the opposite angle dependence implies a negative λ. In both cases, the $(\partial h/\partial x)^1$ term is forbidden due to inversion symmetry $\Delta h(\theta) = \Delta h(-\theta)$.

We next consider the details of the current-driven motion. As depicted in Fig. 2(b), J can be decomposed into the vector components, parallel ($J_\parallel$) and normal ($J_\perp$) to the DW. Since $J_\parallel$ makes no macroscopic change along the normal direction, it is reasonable to assume that $\Delta h_\perp$ is mainly driven by $J_\perp$. Then, by defining the new axes parallel (x') and normal (h') to the DW, it becomes a very typical situation where the DW lies along the horizontal x' axis and the DW is driven by $J_\perp$ along the vertical h' axis as shown by the green window in Fig. 2(b). The creep scaling is then related to the DW roughness in the h' axis, of which the scaling exponent ζ'_J is measured with respect to the x' axis. It is experimentally revealed that ζ'_J is invariant ($= 0.69 \pm 0.04$) irrespective of θ for the range of L smaller than a few tens of micrometers. Note that $\zeta'_J \neq \zeta_J$, which is a common symptom [18] of an interface with facet formation. Interestingly, ζ'_J is identical to ζ_H [4–6]. It is thus natural to infer that the creep scaling in the x'-h' coordinate system is independent of the driving forces with the common creep scaling exponent μ ($=[2\zeta-1]/[2-\zeta]$) given by 1/4 in both cases [3,4]. Therefore, the well-established creep theory can be applied.

For the case that the current is injected normal to the DW in metallic ferromagnetic materials, it has been theoretically proposed [19] and experimentally verified [12] that the DW speed V follows the creep law $V = v_0 \exp[-\alpha\{H^*\}^{-\mu}]$, with respect to the effective field $H^*(H, J) = H - \epsilon J - \eta J^2\sqrt{H - \epsilon J} + (2/5)\eta^2 J^4 + \cdots$, where v_0 is the characteristic speed and α is the ratio of a scaling energy constant over the thermal energy. Here, ϵ and η are the efficiency constants of the nonadiabatic and

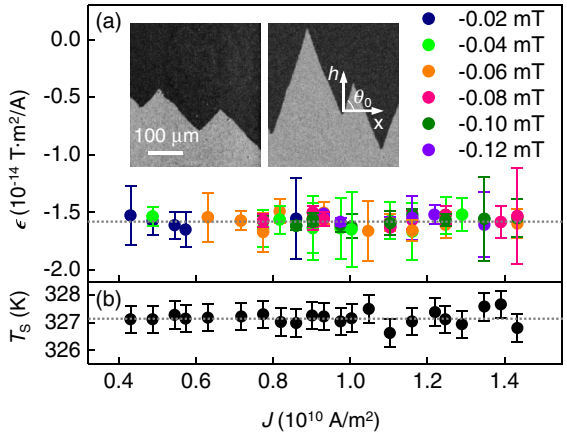

FIG. 3 (color online). (a) Experimentally determined ϵ plotted with respect to J. The symbols with different colors correspond to different H as shown. The error bars correspond to the standard deviation of several θ_0 in each image. The insets show typical stable facet structures for two different H and J. The left inset image is obtained for $H = -0.08$ mT and $J = 0.8 \times 10^{10}$ A/m^2 and the right one is obtained for $H = -0.08$ mT and $J = 1.4 \times 10^{10}$ A/m^2. (b) The sample temperature T_S during the measurement. To reduce the effects from the temperature rise due to the Joule heating, T_S is kept constant (327 $\pm$ 1 K) by controlling the cryostat base temperature, where T_S is estimated from the sample resistance [12]. Note that T_S is set to be a little bit higher than the room temperature for fast DW stabilization.

adiabatic STTs, respectively. Then, for a DW with an angle θ, the creep law can be generalized by simply replacing J by $J_\perp$ ($= J\cos\theta$) as

$$V(H, J; \theta) = \frac{v_0 \exp[-\alpha\{H^*(H, J\cos\theta)\}^{-\mu}]}{\cos\theta}. \quad (1)$$

Experiments on a purely field-driven creep rigorously quantify v_0 ($=14\pm1$ m/s) and α ($=11.6\pm0.2$ mT$^{-1/4}$). To test Eq. (1) for a purely current-driven creep, we adopt ϵ [$=(-1.6\pm0.1)\times10^{-14}$ Tm^2/A] and η [$=(-1.8\pm0.2)\times10^{-24}$ T$^{1/2}$m^4/A^2]. which was reported in Ref. [12] for the same film structure. The red line in Fig. 2(i) shows the theoretical value of $V(H = 0, J; \theta)/V(H = 0, J; 0)$ (i.e., $= \Delta h/\Delta h_0$) and agrees excellently with the experimental results, supporting the validity of Eq. (1) for the current-driven DW motion for an arbitrary θ. Note that no fitting parameter is used, since all the values of v_0, α, ϵ, and η are determined from other independent measurements.

Finally, the facet structure provides a way to rigorously determine ϵ [12,20,21]. For the case that both H and J are applied and their driving forces are opposite to each other, the force from H can be exactly balanced out when $H = \epsilon J_\perp$. Here, $\epsilon J_\perp$ is the effective field caused by the fieldlike nonadiabatic STT [12,19–23]. It thus provides an equilibrium angle θ_0 that satisfies $\cos\theta_0 = H/\epsilon J$. For a mountain with an initial angle other than θ_0, the two driving forces are unbalanced and generate a net restoring force toward θ_0. Thus, the DW spontaneously evolves to a stable facet structure with θ_0. During this process, the adiabatic STT does not affect θ_0 since the adiabatic STT simply reduces the energy barrier of the DW motion, whereas the direction of the DW motion is determined by the balance between the magnetic field and nonadiabatic STT [19].

The stable facet structures as shown in the insets of Fig. 3 clearly demonstrate that the slope of the mountains is the same irrespective of the mountain size. Therefore, each single image unambiguously provides an experimental value of $\epsilon (= H/J\cos\theta_0)$, irrespective of any other experimental situation. It is also worthwhile to note that the same ϵ is obtained for other polarities of the magnetic domains as well as the directions of the current and field [24]. The formation of such facet structure is also confirmed for 3 different samples over the range between 38° and 83° with a typical angle dispersion of 3°. Figure 3 confirms that ϵ is invariant [$= (-1.6 \pm 0.1) \times 10^{-14}$ Tm^2/A], irrespective of H and J. The present results prove the validity of the general assumption used in the theories as well as the experimental analyses on the fieldlike torque, which is currently best explained by the nonadiabatic STT [9,20]. As other possible origins of such fieldlike torque with a linear proportionality on J, the Rashba coupling [25] and the spin Hall effects [26] also have to be examined for our experimental conditions in future studies, though the effect is expected to be small in our samples due to the almost symmetric layer structure.

This work was supported by the National Research Foundation of Korea (NRF) grant funded by the Korea government (MEST) (Grants No. 2012-003418 and No. 2008-0062257). S. C. Y, B. C. M., and K. H. S. were supported by the KIST institutional program and pioneer research center program (2011-0027905) through NRF funded by MEST.

*sugbong@snu.ac.kr

[1] K.-S. Ryu, H. Akinaga, and S.-C. Shin, Nat. Phys. **3**, 547 (2007).
[2] D.-H. Kim, S.-B. Choe, and S.-C. Shin, Phys. Rev. Lett. **90**, 087203 (2003).
[3] P. Chauve, T. Giamarchi, and P. Le Doussal, Phys. Rev. B **62**, 6241 (2000).
[4] S. Lemerle, J. Ferré, C. Chappert, V. Mathet, T. Giamarchi, and P. Le Doussal, Phys. Rev. Lett. **80**, 849 (1998).
[5] D. A. Huse and C. L. Henley, Phys. Rev. Lett. **54**, 2708 (1985).
[6] M. Kardar and D. R. Nelson, Phys. Rev. Lett. **55**, 1157 (1985).
[7] K.-J. Kim, J.-C. Lee, S.-M. Ahn, K.-S. Lee, C.-W. Lee, Y. J. Cho, S. Seo, K.-H. Shin, S.-B. Choe, and H.-W. Lee, Nature (London) **458**, 740 (2009).
[8] G. Tatara and H. Kohno, Phys. Rev. Lett. **92**, 086601 (2004).

[9] S. Zhang and Z. Li, Phys. Rev. Lett. **93**, 127204 (2004).
[10] A. Thiaville, Y. Nakatani, J. Miltat, and Y. Suzuki, Europhys. Lett. **69**, 990 (2005).
[11] M. Yamanouchi, J. Ieda, F. Matsukura, S. E. Barnes, S. Maekawa, and H. Ohno, Science **317**, 1726 (2007).
[12] J.-C. Lee, K.-J. Kim, J. Ryu, K.-W. Moon, S.-J. Yun, G.-H. Gim, K.-S. Lee, K.-H. Shin, H.-W. Lee, and S.-B. Choe, Phys. Rev. Lett. **107**, 067201 (2011).
[13] A.-L. Barabási and H. E. Stanley, *Fractal Concepts in Surface Growth* (Cambridge University Press, Cambridge, 1995).
[14] M. Kardar, G. Parisi, and Y. C. Zhang, Phys. Rev. Lett. **56**, 889 (1986).
[15] L.-H. Tang and H. Leschhorn, Phys. Rev. A **45**, R8309 (1992).
[16] H. Jeong, B. Kahng, and D. Kim, Phys. Rev. Lett. **77**, 5094 (1996).
[17] H. Jeong, B. Kahng, and D. Kim, Phys. Rev. E **59**, 1570 (1999).
[18] H.-W. Lee and D. Kim, Phys. Rev. E **56**, R2347 (1997).
[19] J. Ryu, S.-B. Choe, and H.-W. Lee, Phys. Rev. B **84**, 075469 (2011).
[20] O. Boulle, J. Kimling, P. Warnicke, M. Kläui, U. Rüdiger, G. Malinowski, H. J. M. Swagten, B. Koopmans, C. Ulysse, and G. Faini, Phys. Rev. Lett. **101**, 216601 (2008).
[21] I. M. Miron, P.-J. Zermatten, G. Gaudin, S. Auffret, B. Rodmacq, and A. Schuhl, Phys. Rev. Lett. **102**, 137202 (2009).
[22] L. Thomas, M. Hayashi, X. Jiang, R. Moriya, C. Rettner, and S. S. P. Parkin, Nature (London) **443**, 197 (2006).
[23] S.-W. Jung, W. Kim, T.-D. Lee, K.-J. Lee, and H.-W. Lee, Appl. Phys. Lett. **92**, 202508 (2008).
[24] J. Heinen, O. Boulle, K. Rousseau, G. Malinowski, M. Kläui, H. J. M. Swagten, B. Koopmans, C. Ulysse, and G. Faini, Appl. Phys. Lett. **96**, 202510 (2010).
[25] I. M. Miron, K. Garello, G. Gaudin, P.-J. Zermatten, M. V. Costache, S. Auffret, S. Bandiera, B. Rodmacq, A. Schuhl, and P. Gambardella, Nature (London) **476**, 189 (2011).
[26] L. Liu, C.-F. Pai, Y. Li, H. W. Tseng, D. C. Ralph, and R. A. Buhrman, Science **336**, 555 (2012).